Compact silicon diffractive sensor: design, fabrication, and prototype

Jonathan S. Maikisch* and Thomas K. Gaylord

School of Electrical and Computer Engineering, Georgia Institute of Technology, Atlanta, Georgia 30332-0250, USA

*Corresponding author: Jonathan.Maikisch@gatech.edu

Received 4 April 2012; accepted 21 May 2012;
posted 23 May 2012 (Doc. ID 166015); published 25 June 2012

An in-plane constant-efficiency variable-diffraction-angle grating and an in-plane high-angular-selectivity grating are combined to enable a new compact silicon diffractive sensor. This sensor is fabricated in silicon-on-insulator and uses telecommunications wavelengths. A single sensor element has a micron-scale device size and uses intensity-based (as opposed to spectral-based) detection for increased integrability. In-plane diffraction gratings provide an intrinsic splitting mechanism to enable a two-dimensional sensor array. Detection of the relative values of diffracted and transmitted intensities is independent of attenuation and is thus robust. The sensor prototype measures refractive index changes of 10^{-4}. Simulations indicate that this sensor configuration may be capable of measuring refractive index changes three or four orders of magnitude smaller. The characteristics of this sensor type make it promising for lab-on-a-chip applications.

OCIS codes: 050.1950, 130.0130, 130.6010.

1. Introduction

Optical lab-on-a-chip (LOAC) sensors offer significant advantages for applications in medicine, food safety, environmental monitoring, defense, and homeland security, all requiring robust and highly sensitive detection. An optical measurement is inherently immune to electromagnetic interference (EMI), and resonant measurements provide a high degree of sensitivity. Optical sensors typically respond to changes in refractive index, avoiding electrical interaction with the analyte and providing label-free sensing. These advantages are critical in meeting the commercial demand for field-deployable LOAC devices. Field-deployable devices require small device sizes, integrated functionality (fluid delivery, source, detection, and data acquisition), and multiplex capability. Recent work has been devoted to developing robust integrated detection platforms with high sensitivity for multiplexed and redundant sensing [1–4].

Various optical sensor platforms for LOAC integration have extensively been investigated in the literature. The most promising and relevant of these technologies include surface plasmon resonance (SPR) [1–5], Mach—Zehnder interferometers (MZI) [6–10], and microring resonators [3,11–14]. SPR sensors offer moderate sensitivities up to 10^{-5} refractive index units (RIU) but have interaction lengths typically on the order of millimeters [4,5]. MZI sensors offer enhanced sensitivity at the expense of larger device sizes. Typical interaction lengths to achieve sensitivities in excess of 10^{-5} RIU are on the order of 10 mm [6–8]. With microring resonator sensors, the device sensitivity is mainly influenced by the quality factor [3,12,13]. While theoretical microring devices can achieve extremely high quality factors, they are often limited by fabrication tolerances. Devices have been shown to achieve sensitivities on the order of 10^{-5} RIU with device diameters of tens of microns [12,13]. Sensitivities approaching 10^{-7} RIU have been predicted with further improvements [11–13]. SPR, MZI, and microring resonator sensors can operate with integrated intensity-based (as opposed to spectral-based) detection. This type of

1559-128X/12/194325-08$15.00/0

measurement is based on the output attenuation of a monochromatic source. However, SPR and microring resonator sensors typically operate with spectral-based detection to maximize sensitivity. These sensor types can be arranged in linear arrays for multiplexed sensing but would require complex geometries and the addition of optical splitters to enable two-dimensional (2D) arrays with intensity-based detection.

There is a need for a robust integrated optical sensing platform with micron-scale device sizes, intensity-based detection, and 2D sensor array capability. Micron-scale device sizes allow for dense population of sensors for multiplexed and redundant sensing. Intensity-based detection brings down cost and enables use of integrated photodetectors. However, attenuation measurements are susceptible to degradation of the optical signal. A robust platform should offer intensity-based measurement that is unaffected by source fluctuations. Integration in a 2D sensor array requires linear sequences of sensors to share source power. Ideally, this would be accomplished without additional optical splitters and complex geometries. In addition to these features, the platform must exhibit high sensitivity and robust operation while minimizing cost and fabrication difficulty.

The new class of compact silicon diffractive sensors (CSDS) described here is silicon-on-insulator (SOI) based to limit costs, to exploit established fabrication processes, to allow for integration with additional electronics, and to utilize the well-understood telecommunications wavelength of 1.55 μm. Sensing is achieved by combining constant-diffraction-efficiency and highly angularly selective in-plane resonance-domain diffraction gratings. Detection is based on the diffraction efficiency of the highly angularly selective grating. In-plane diffraction gratings offer many advantages for integrated optical sensing. Device sizes are small, with grating thicknesses typically only a few microns. Detection is intensity based. Further, the relative values of the diffracted intensity and the transmitted intensity are independent of attenuation in the system. Also, the use of in-plane diffraction gratings allows for source light to be shared by linear arrays of sensors without additional optical splitters. This intrinsic splitting mechanism enables compact 2D arrays of sensors for multiplexed and redundant sensing. This new approach provides multiplexed and redundant sensing capability for field-deployable LOAC applications without sacrificing sensitivity or robustness.

2. Sensor Configuration

The new class of CSDS described here utilizes two in-plane diffraction gratings, a primary grating and a secondary grating, as depicted in Fig. 1. The primary grating is designed to have constant diffraction efficiency with a variable diffraction angle. It is bounded by an immobilization layer. Target analyte is delivered by the fluid input microchannel and immobilized.

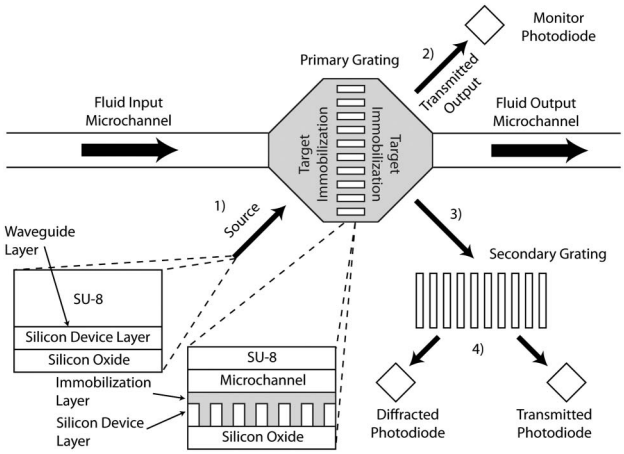

Fig. 1. CSDS platform operation and structure. (1) Source light is incident upon the primary grating. (2) Partial transmission to a monitor photodiode or an additional sensor element. (3) Diffraction toward the secondary grating at an angle dependent on analyte immobilization. (4) Measured diffraction and transmission at the secondary grating.

This alters the refractive index surrounding the grating. The secondary grating is designed to be highly angularly selective. It is oriented to accept light diffracted by the primary grating. Operation of the CSDS platform proceeds as shown in Fig. 1: (1) Source light passes under the immobilization layer and is incident upon the primary grating. (2) A fixed portion of the incident light is transmitted through the primary grating toward a monitor photodiode or another CSDS sensor in a linear sensor array. (3) The remaining portion of light is diffracted by the primary grating toward the secondary grating. The diffracted angle is sensitively dependent on the refractive index surrounding the primary grating. (4) Light incident upon the highly angularly selective secondary grating is both diffracted and transmitted. The diffraction efficiencies are determined by the incident angle and the corresponding amount of analyte immobilized. This light is detected by the appropriate photodiodes and related to the analyte concentration.

The layer structure of the CSDS sensor is illustrated in Fig. 1. Source light at the telecommunications wavelength of $\lambda = 1.55$ μm is confined to the fundamental slab mode of the silicon device layer on the SOI wafer. The light is linearly polarized with the electric field orientation perpendicular to the layer interfaces. This polarization is necessary to maximize forward diffraction efficiencies and to minimize backward diffraction efficiencies. Gratings and photodiodes are fabricated in the silicon device layer of the SOI wafer, allowing for use of mature silicon processing technologies. The microfluidic channel is fabricated in the polymer cladding layer for analyte delivery. A thin immobilization layer is deposited on the region bounding and covering the primary grating within the microfluidic channel.

Realization of a compact 2 D sensor array for LOAC applications is depicted in Fig. 2. Source light is incident upon several one-dimensional (1D) linear

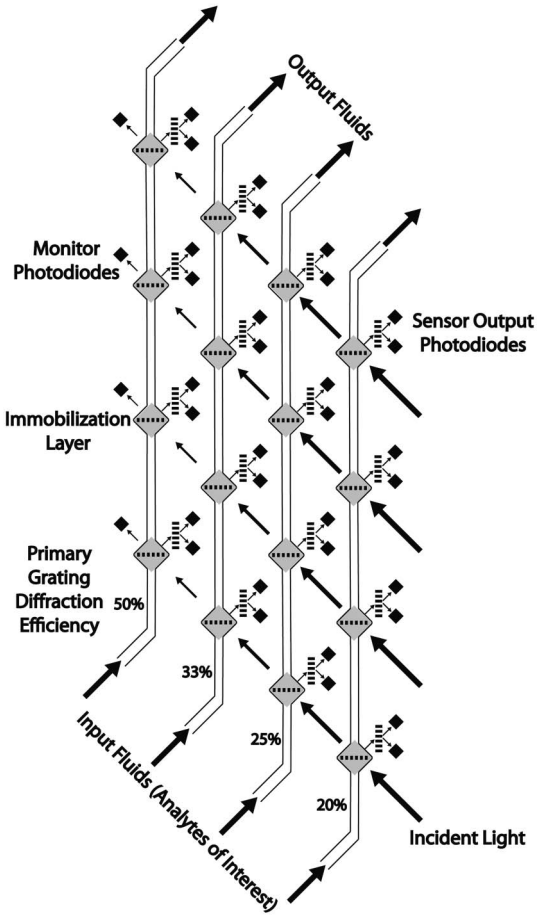

Fig. 2. Compact 2D CSDS sensor array. In each linear array of sensors, the primary grating diffraction efficiencies are 20%, 25%, 33%, and 50%, respectively. This provides 20% of the source power in each linear sequence to the secondary gratings. Monitor photodiodes are included at the end of each sensor sequence to increase device robustness.

arrays of CSDS sensors. In each linear array, the primary grating diffraction efficiencies are 20%, 25%, 33%, and 50%, respectively, for this case of four sensors for each source. An even distribution of the incident source power (20%) is provided to each secondary grating. Microfluidic channels deliver the fluid under test to each row of bounded primary gratings. This enables delivery of various test fluids to multiple sensors for multiplexed and redundant sensing. Monitor photodiodes at the end of each linear CSDS array monitor the intended 20% of incident source power. This provides for a full accounting of the light in the 2D CSDS array. This configuration best illustrates the advantages of the CSDS platform's intrinsic splitting mechanism in enabling compact 2D sensor arrays.

The test analyte for proof-of-concept of the CSDS platform is anticipated to be toluene, since it is well understood and relatively easy to handle. Immobilization of toluene will be achieved via free-volume filling with a 30 nm layer of poly n-butyl-isobutyl methacrylate (PBIBMA). High-glass-transition-temperature polymers, such as PBIBMA and Teflon AF have been shown to work well for toluene with this mechanism [15]. With free-volume filling, the analyte of interest is trapped in interstitial spaces within the immobilization layer, modifying the refractive index. For the polymer cladding and microchannel infrastructure, SU-8 from MicroChem [16] in the 2002 formulation is chosen for its mechanical and thermal stability. The indices of refraction of SU-8 and PBIBMA after deposition have been determined to be 1.581 and 1.471 respectively via ellipsometry. SOI wafers from Soitec [17] have a nominal 250 nm silicon device layer and a 3 μm buried oxide layer. The calculated effective indices for the slab waveguide modes [18] are 2.305 and 2.341 for PBIBMA and SU-8 claddings, respectively.

3. Design and Simulation

The primary grating configuration with boundaries is depicted in Fig. 3. The incident and diffracted angles, θ and θ_m, respectively, are both chosen to be 45°. This allows for sensor elements to be orientated at right angles, simplifying fabrication and layout of a 2D array as in Fig. 2. The boundary orientation angles, α and α_m, are also chosen to be 45°. This minimizes dephasing from the Bragg condition to maintain constant diffraction efficiency and provides suitable output angle variation with variation of the cladding refractive index.

To determine the primary grating thickness, d, and fill factor, F, rigorous coupled-wave analysis (RCWA) [19–22] was used with plane-wave incidence. Comparisons to finite-difference time-domain (FDTD) simulation using the MIT Electromagnetic Equation Propagation (MEEP) engine [23] with Gaussian beams with a 2 μm beam waist show differences to be less than 1%. Diffraction efficiencies for backward orders are designed to be less than 0.1% with RCWA and confirmed to be less than 0.1% with FDTD Gaussian analysis. The agreement between the two analyses extends to sensitivity analysis for grating thickness, fill factor, surrounding refractive index, and incident angle. This indicates that RCWA

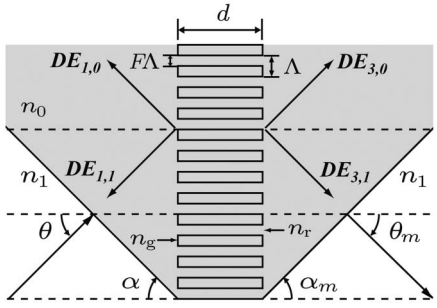

Fig. 3. Bounded primary grating configuration. Grating parameters include the thickness, d, period,Λ, and fill factor, F. The incident and diffracted angles outside the bounded area are θ and θ_m. The boundary orientation angles are α and α_m. The refractive index within the boundary is n_0 and the surrounding refractive index is n_1. The grating ridge and groove indices are n_r and n_g. Forward diffracted and transmitted orders are $DE_{3,1}$ and $DE_{3,0}$ Backward diffracted and reflected orders are $DE_{1,1}$ and $DE_{1,0}$.

is suitably accurate for primary grating design. The primary grating designs and simulation results are presented in Table 1.

The secondary grating requires a linear, monotonic change in diffraction efficiency as the incident angle is varied. The diffraction efficiency response when operating near a Bragg condition is broad and symmetric. To meet these criteria, the secondary grating needs to operate at a controlled angular shift, θ_{bias}, from the Bragg condition. Overall sensor sensitivity depends on the angular selectivity of the secondary grating. Careful design of the secondary grating is necessary to achieve high sensitivity with readily achievable fabrication tolerances. For layout considerations similar to those for the primary grating, the incident and diffracted angles are chosen as $\theta = \theta_m = 45°$. Unlike the primary grating, there are no boundaries ($n_0 = n_1 = 2.341$) as the entire area is clad by the same material (SU-8 in this case).

Grating period, Λ; thickness, d; and fill factor, F are determined via RCWA simulation. The design for the secondary grating is presented in Table 1. The angular response for the designed secondary grating is plotted in Fig. 4. At $\theta = \theta_{\text{bias}} = 41.65°$, the Bragg condition is fulfilled for 100% diffraction efficiency and the desired behavior is achieved at the designed incident angle, $\theta = 45°$. The angular responsivity simulated with RCWA is 21.35%/deg. Comparisons of RCWA with FDTD Gaussian analysis differ less than 5% for the forward diffracted orders and 0.5% for the backward diffracted orders. This level of agreement extends to sensitivity analysis for grating thickness, fill factor, and surrounding refractive index. The effect of Gaussian incidence is apparent when considering the sensitivity to incident angle in Fig. 4. The angular sensitivity for the FDTD Gaussian analysis is determined to be 13.92%/deg. This is a 7.43%/deg decrease from the angular selectivity obtained with RCWA. The additional angular components from a Gaussian beam inherently decrease the angular selectivity. It is important to note that the desired linear, monotonic behavior is still achieved about the proper incident angle of 45°. This behavior is expected and again indicates that RCWA is an effective and efficient tool for this design process.

Since it has been shown that Gaussian incidence has a significant effect on the performance of the secondary grating, sensor performance is analyzed by FDTD with Gaussian incidence. This analysis is done for all of the primary grating designs. The refractive index of the immobilization layer (PBIBMA) was varied by ± 0.01 and the effective indices are recalculated. The sensor responsivity is simulated to be −0.692%/mRIU. Taking a typical source power of 1 mW divided among four sensors and a monitor photodiode in a linear sensor array, the incident power is taken as 0.2 mW per sensor. With a published SOI photodetector responsivity of 0.8 A/W [24], the sensor resolution is calculated to be 10^{-8} RIU. This number neglects detector noise but provides an upper limit for the platform sensitivity. Since the secondary grating is designed to operate linearly, this would also be the minimum detectable level. Further gains in sensitivity can be made with secondary grating designs that have smaller fabrication tolerances. This upper limit on sensor resolution indicates that the CSDS platform is capable of the sensitivities required by LOAC applications.

4. Fabrication

The primary and secondary gratings are fabricated with electron beam lithography (EBL). The gratings are patterned with ZEP-520A from Zeon Chemicals [25]. The grating patterns are transferred to the silicon device layer via a nanoscale inductively coupled plasma (ICP) Bosch process [26]. This etching technique is chosen since it produces nearly vertical sidewalls and has a high etch selectivity of 8:1 (Silicon: ZEP). Vertical sidewalls yield a constant fill factor at the top and bottom of the grating grooves. This is important to achieve the designed grating characteristics. The high etch selectivity allows for a thinner ZEP mask, which reduces the aspect ratio and

Table 1. Designs for Primary and Secondary Gratings Simulated with RCWA (Plane-Wave Incidence) and FDTD (Gaussian Incidence) Analyses

Primary Grating ($\lambda = 1.55\ \mu$m, $\Lambda = 0.475\ \mu$m, $n_1 = 2.341$, $n_0 = n_r = 2.305$, $n_g = 1.471$)						
Grating Parameters			*Diffraction Efficiencies*			
Target diffraction efficiency	Thickness $d(\mu$m)	Fill factor F	Diffracted $DE_{3,1}$ (%)	Transmitted $DE_{3,0}$ (%)	Backward diffracted $DE_{1,1}$ (%)	Reflected $DE_{1,0}$ (%)
20% RCWA	0.615	0.811	20.02	79.98	0.00	0.00
20% FDTD			19.85	80.10	0.01	0.04
25% RCWA	0.636	0.794	25.00	75.00	0.00	0.00
25% FDTD			24.75	75.20	0.00	0.05
33% RCWA	0.668	0.770	33.33	66.67	0.00	0.00
33% FDTD			32.90	67.03	0.00	0.07
50% RCWA	0.725	0.731	50.00	50.00	0.00	0.00
50% FDTD			49.10	50.77	0.01	0.12
Secondary grating ($\lambda = 1.55\ \mu$m, $\Lambda = 0.498\ \mu$m, $n_0 = n_1 = n_r = 2.341$, $n_g = 1.581$)						
RCWA	3.105	0.852	52.50	47.03	0.20	0.27
FDTD			48.00	51.39	0.22	0.39

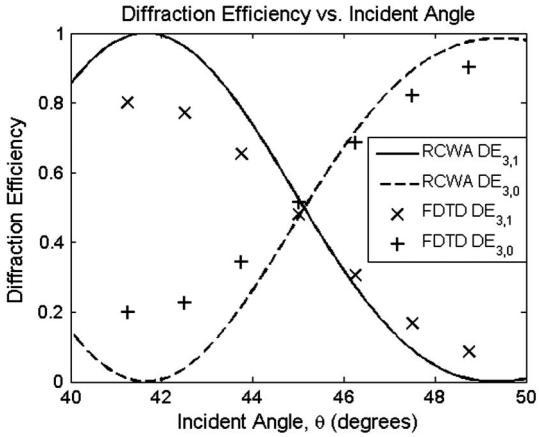

Fig. 4. Angular sensitivity of the secondary grating simulated with RCWA (plane-wave incidence) and FDTD (Gaussian incidence). The desired linear, monotonic behavior is achieved about the incident angle $\theta = 45°$ Backward orders, $DE_{1,1}$ and $DE_{1,0}$, are negligible.

prevents sidewall collapse. A fabricated secondary grating is depicted in Fig. 5. This process repeatedly yields fabricated grating features that are within 1% of the designed values. After transfer of the grating patterns, the photodetectors can be fabricated in the silicon device layer. For large-scale manufacturing, the gratings could be fabricated via nanoimprint lithography (NIL) with a stamp patterned by EBL. NIL has been shown to be suitable for fabrication of features of the required size [27–30]. This provides a low-cost, high-throughput fabrication, which is necessary for development of a field-deployable LOAC sensing platform.

Definition of the primary grating boundary and the microchannels is done in the SU-8 cladding with optical lithography. The immobilization layer (PBIB-MA) is then deposited on the primary grating. The sensor is then capped with an oxygen-plasma-treated polydimethysiloxane (PDMS) sheet to complete the microchannels [31]. More permanent microchannels can be fabricated by filling the microchannels with a sacrificial polymer. This polymer and the surrounding SU-8 cladding are then machined down to the desired microchannel height. An additional SU-8 cladding layer is then deposited to cover the microchannel. The wafer is then heated, allowing the sacrificial polymer to evacuate [32,33] and completing microchannel fabrication.

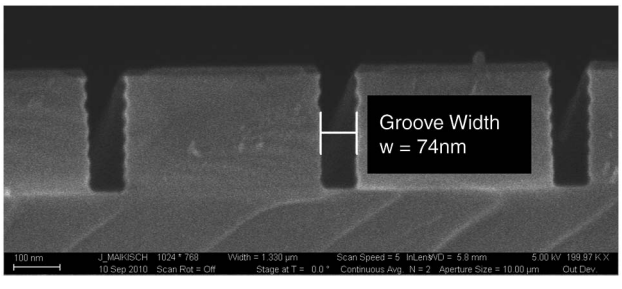

Fig. 5. Scanning electron microscope image of a fabricated secondary grating crosssection. The nanoscale ICP Bosch process used achieves nearly vertical sidewalls and feature sizes within 1% of target values.

5. Experimental Results

Characterization of the CSDS primary and secondary gratings requires a robust experimental configuration. A vertical detection scheme is preferable to an in-plane configuration. This allows use of an infrared camera to detect simultaneously all the diffracted orders. This relieves the limitations of using multiple external photodetectors. To accomplish this, vertical outcoupling gratings are designed with cavity modeling framework (CAMFR) software [34]. Also, light incident upon the gratings must be a slab-confined beam with finite width. Coupling of light into the SOI piece requires use of a 2D waveguide. The transition from the 2D input waveguide to the 1D slab structure must minimize beam divergence and radiative loss. Input waveguides are designed with FDTD simulation.

The experimental configuration is illustrated in Fig. 6. Monochromatic light at 1550 nm is provided by a tunable laser. The source light polarization is controlled by a polarization controller. Light is coupled into the input waveguide by a tapered fiber. Diffracted light is coupled out of the sample by the outcoupling gratings and imaged by a microscope objective. The image is then recorded by an infrared camera for analysis. The measured diffraction efficiency is defined here as, $I_{3,1}/(I_{1,0} + I_{3,0} + I_{3,1})$ where $I_{3,1}$ is the diffracted intensity, $I_{3,0}$ is the transmitted intensity, and $I_{1,0}$ is the reflected intensity.

The primary grating designs are fabricated in the configuration shown in Fig. 7. Light is shaped by the input waveguide and is incident upon the grating. Outcoupling gratings capture the diffracted, transmitted, and reflected light for detection. A 100 μm

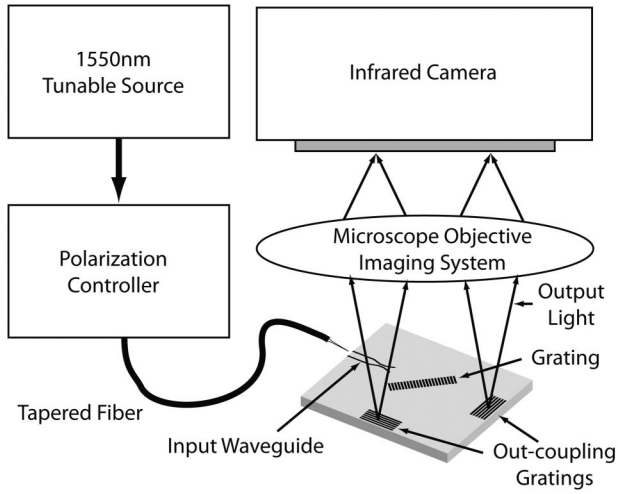

Fig. 6. Experimental configuration for grating and sensor characterization. Polarization-controlled monochromatic light is coupled to the sample by tapered fiber. After diffraction by the element under test, light is coupled out-of-plane by out-coupling gratings. It is then imaged by a microscope objective to an infrared camera for measurement.

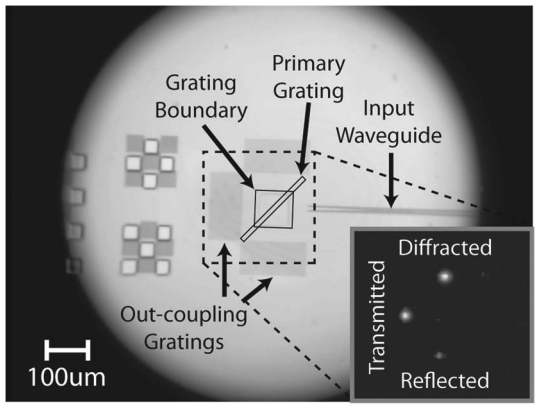

Fig. 7. Fabricated primary grating experimental configuration and measurement for the 50% primary grating with the $n = 1.432$ refractive index oil within the grating boundary.

square is defined in the SU-8 cladding for the grating boundary. Refractive index oils with indices ranging from 1.432 to 1.511 were flowed in the grating boundary region. Experimental results are compared with FDTD simulation with Gaussian incidence. Results for the primary grating design with 50% diffraction efficiency are presented in Fig. 8. The efficiency of the diffracted order is in good agreement with the simulations. There is a small reflection, but this does not affect the diffraction efficiency. This demonstrates that the primary gratings serve the designed function in the CSDS platform.

The secondary grating is fabricated in a configuration similar to that of the primary grating. The primary difference is that there is no grating boundary and the entire device is clad with SU-8. Light is incident upon the secondary grating at angles ranging from $\theta = 43°$ to 47° in increments. Bends in the input waveguides orient incident light to the desired angle. Experimental results are compared with FDTD simulation with Gaussian incidence in Fig. 8. The efficiency of the diffracted order is in good agreement with the simulations. The desired linear, monotonic behavior is observed. As with the primary grating, there is reflection, but it does not affect the measured diffraction efficiency. This demonstrates that the secondary grating serves the designed function in the CSDS platform.

The CSDS sensor with each primary grating design and the secondary grating design is fabricated in the configuration shown in Fig. 9. Refractive index oils with indices ranging from 1.432 to 1.511 were flowed in the boundary region of the primary grating. Experimental results are compared with FDTD simulation with Gaussian incidence. Results for the sensor with a 50% primary grating design are presented in Fig. 8. The simulation results are adjusted for the measured thickness of the silicon device layer (253 nm). This thickness has a negligible effect on the characteristic grating diffraction efficiency but a more significant effect on the diffracted angle at the primary grating. The measured diffraction efficiency at the secondary grating is in excellent agreement

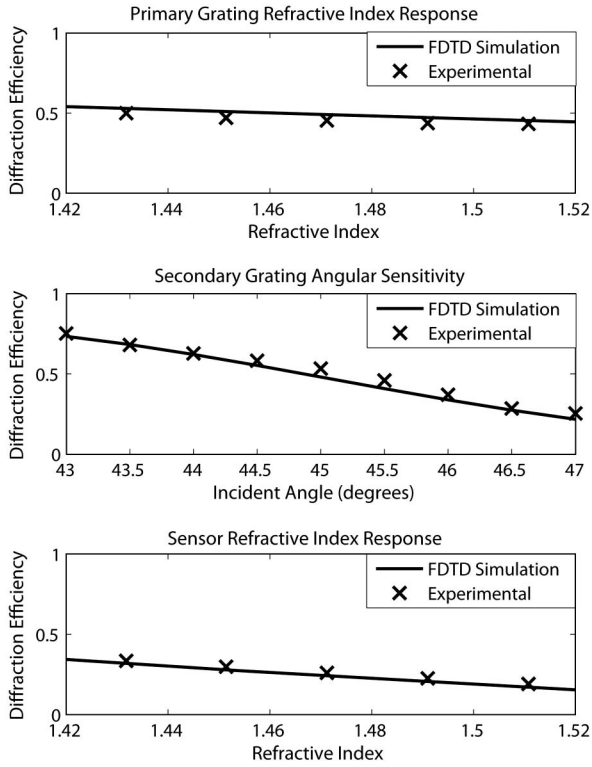

Fig. 8. Experimental results compared with FDTD simulation with Gaussian incidence for the 50% primary grating refractive index response (top), secondary grating angular sensitivity (middle), and sensor (with the 50% primary grating) refractive index response (bottom). For the primary grating and sensor responses, refractive index oils ranging from $n = 1.432$ to $n = 1.511$ were flowed into the primary grating boundary. For the secondary grating, several gratings are fabricated with input waveguides that provide incident angles ranging from $\theta = 43°$ to $\theta = 47°$. The diffraction efficiencies are in good agreement with simulation.

with the FDTD simulation. The estimated sensitivity of this experimental configuration is 10^{-4} RIU. This sensitivity is primarily limited by noise in the infrared camera. Sensitivities approaching the simulated capability of 10^{-8} RIU may be possible with integrated photodiodes and other refinements. These preliminary experimental results show the CSDS platform successfully detecting the changes in the

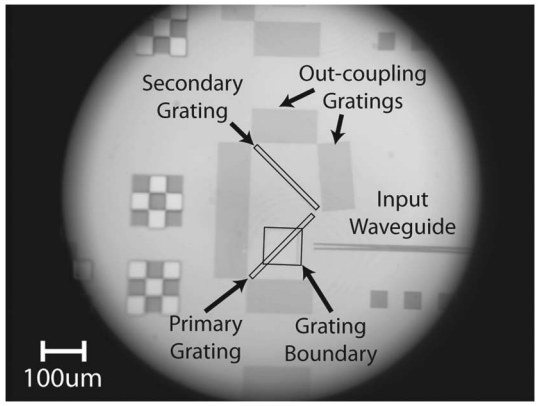

Fig. 9. Fabricated experimental configuration to characterize the CSDS sensor.

cladding refractive index within the primary grating boundary.

6. Summary and Discussion

In this article, a new class of CSDS for LOAC applications is presented. This configuration consists of an in-plane constant-efficiency variable-diffraction-angle grating combined with an in-plane high angular-selectivity grating. This class of sensors is noteworthy in that it offers micron-scale device sizes, attenuation-independent intensity-based (as opposed to spectral-based) detection, and 2D sensor array capability. Micron-scale device sizes allow for dense population of sensors for multiplexed and redundant sensing. Intensity-based detection brings down cost and enables use of integrated photodetectors. Detection of the relative values of the diffracted and transmitted intensities is independent of attenuation and is thus insensitive to possible source fluctuations. The intrinsic splitting capability enables linear sequences of sensors to share source power. These linear sensor arrays can be combined into a 2D sensor array without the addition of optical splitters and complex geometries. The SOI substrate allows for use of mature fabrication processes and telecommunications wavelengths while minimizing cost. Simulation indicates a sensitivity capability that meets the demands of LOAC applications. Overall sensor resolution is strongly dependent on the angular selectivity of the secondary grating, and can be further enhanced as fabrication capabilities improve.

Experimental characterization of the individual in-plane gratings shows excellent agreement with the simulated designs. Characterization of the sensor response with refractive index oils also shows excellent agreement with simulation. These results show that the CSDS platform is capable of detecting changes in the cladding refractive index. Work is ongoing to demonstrate this capability in a linear sequence of sensors. This will exploit the intrinsic splitting capability of the CSDS platform and form the basis for 2D sensor arrays. There is also ongoing work to integrate microfluidic channels and the PBIBMA immobilization layer for the proof-of-concept toluene sensor. These experiments will show that the CSDS sensor is capable of producing high-sensitivity, robust refractive index sensors for field-deployable LOAC applications.

References

1. P. Adam, J. Dostalek, and J. Homola, "Multiple surface plasmon spectroscopy for study of biomolecular systems," Sensor. Actuat. B-Chem. **113**, 774–781 (2006).
2. J. Homola, *Surface Plasmon Resonance Based Sensors*, Springer Series on Chemical Sensors and Biosensors (Springer, 2006), Vol. **4**.
3. P. Debackere, D. Taillaert, K. De Vos, S. Scheerlinck, P. Bienstman, and R. Baets, "Si based waveguide and surface plasmon sensors," Proc. SPIE **6477**, 647719 (2007).
4. J. R. Krenn, N. Galler, H. Ditlbacher, A. Hohenau, B. Lamprecht, E. Kraker, G. Jakopic, and T. Mayr, "Waveguide-integrated SPR sensing on an all-organic platform," Proc. SPIE **8073**, 80730F (2011).
5. R. D. Harris and J. S. Wilkinson, "Waveguide surface plasmon resonance sensors," Sensor. Actuat. B-Chem. **29**, 261–267 (1995).
6. F. Prieto, B. Sepulveda, A. Calle, A. Llobera, C. Dominguez, A. Abad, A. Montoya, and L. M. Lechuga, "An integrated optical interferometric nanodevice based on silicon technology for biosensor applications," Nanotech. **14**, 907–912 (2003).
7. L. M. Lechuga, K. Zinoviev, L. Fernandez, J. Elizalde, O. E. Hidalgo, and C. Dominguez, "Biosensing microsystem platforms based on the integration of Si Mach-Zehnder interferometer, microfluidics and grating couplers," Proc. SPIE **7220**, 72200L (2009).
8. B. Sepulveda, J. S. del Rio, M. Moreno, F. J. Blanco, K. Mayora, C. Dominguez, and L. M. Lechuga, "Optical biosensor microsystems based on the integration of highly sensitive Mach-Zehnder interferometer devices," J. Opt. A-Pure Appl. Op. **8**, 561–566 (2006).
9. L. U. Kempen and R. E. Kunz, "Replicated Mach-Zehnder interferometers with focusing grating couplers for sensing applications," Sensor. Actuat. B-Chem. **39**, 295–299 (1997).
10. B. Y. Shew, Y. C. Cheng, and Y. H. Tsai, "Monolithic SU-8 micro-interferometer for biochemical detections," Sensor. Actuat. A-Phys. **141**, 299–306 (2008).
11. M. Iqbal, M. A. Gleeson, B. Spaugh, F. Tybor, W. G. Gunn, M. Hochberg, T. Baehr-Jones, R. C. Bailey, and L. C. Gunn, "Label-free biosensor arrays based on silicon ring resonators and high-speed optical scanning instrumentation," IEEE J. Sel. Top. Quantum Electron. **16**, 654–661 (2010).
12. C.-Y. Chao, W. Fung, and L. J. Guo, "Polymer microring resonators for biochemical sensing applications," IEEE J. Sel. Top. Quantum Electron. **12**, 134–142 (2006).
13. K. De Vos, I. Bartolozzi, E. Schacht, P. Bienstman, and R. Baets, "Silicon-on-insulator microring resonator for sensitive and label-free biosensing," Opt. Express **15**, 7610–7615 (2007).
14. J. Flueckiger, S. M. Grist, G. Bisra, L. Chrostowski, and K. C. Cheung, "Cascaded silicon-on-insulator microring resonators for the detection of biomolecules in PDMS microfluidic channels," Proc. SPIE **7929**, 79290I (2011).
15. D. P. Campbell, J. L. Moore, J. M. Cobb, N. F. Hartman, B. H. Schneider, and M. G. Venugopal, "Optical system-on-a-chip for chemical and biochemical sensing: the chemistry," Proc. SPIE **3540**, 153–161 (1999).
16. MicroChem Corp., Newton, Mass., www.microchem.com.
17. Soitec, Bernin, France, www.soitec.com.
18. H. Kogelnik and V. Ramaswamy, "Scaling rules for thin-film optical waveguides," Appl. Opt. **13**, 1857–1862 (1974).
19. J. S. Maikisch and T. K. Gaylord, "Optimum parallel-face slanted surface-relief gratings," Appl. Opt. **46**, 3674–3681 (2007).
20. S.-D. Wu, T. K. Gaylord, J. S. Maikisch, and E. N. Glytsis, "Optimization of anisotropically etched silicon surface-relief gratings for substrate-mode optical interconnects," Appl. Opt. **45**, 15–21 (2006).
21. M. G. Moharam and T. K. Gaylord, "Rigorous coupled-wave analysis of planar-grating diffraction," J. Opt. Soc. Am. **71**, 811–818 (1981).
22. E. N. Glytsis and T. K. Gaylord, "Three-dimensional (vector) rigorous coupled-wave analysis of anisotropic grating diffraction," J. Opt. Soc. Am. A **7**, 1399–1420 (1990).
23. A. F. Oskooi, D. Roundy, M. Ibanescu, P. Bermel, J. D. Joannopoulos, and S. G. Johnson, "MEEP: A flexible free-software package for electromagnetic simulations by the FDTD method," Comput. Phys. Commun. **181**, 687–702 (2010).
24. M. W. Geis, S. J. Spector, M. E. Grein, R. T. Schulein, J. U. Yoon, D. M. Lennon, S. Deneault, F. Gan, F. X. Kaertner, and T. M. Lyszczarz, "CMOS-compatible all-Si high-speed waveguide photodiodes with high responsivity in near-infrared communication band," IEEE Photon. Technol. Lett. **19**, 152–154 (2007).
25. Zeon Chemicals L. P., Louisville, Ky., www.zeonchemicals.com.
26. D. K. Brown, "Nanometer scale Bosch process silicon etching," presented at IEEE Electron Ion Photon Beam and Nanofabrication Conference, Anchorage, Alaska, June 2010.
27. B. Lu, S.-Q. Xie, J. Wan, R. Yang, Z. Shu, X.-P. Qu, R. Liu, Y. Chen, and E. Huq, "Applications of nanoimprint lithography

for biochemical and nanophotonic structures using SU-8," Int. J. Nanosci. Ser. **8**, 151–155 (2009).
28. S.-Q. Xie, B.-R. Lu, Y. Sun, Y. Chen, X.-P. Qu, and R. Liu, "Fabrication of 150 nm half-pitch grating templates for nanoimprint lithography," J. Nanosci. Nanotechnol. **9**, 1437–1440 (2009).
29. S.-Q. Xie, J. Wan, B.-R. Lu, Y. Sun, Y. Chen, X.-P. Qu, and R. Liu, "A nanoimprint lithography for fabricating SU-8 gratings for near-infrared to deep-UV application," Microelectron. Eng. **85**, 914–917 (2008).
30. M. Yanagisawa, Y. Tsuji, H. Yoshinaga, N. Kono, and K. Hiratsuka, "Evaluation of nanoimprint lithography as a fabrication process of phase-shifted diffraction gratings of distributed feedback laser diodes," J. Vac. Sci. Technol. B **27**, 2776–2780 (2009).
31. J. Ou, T. Glawdel, C. L. Ren, and J. Pawliszyn, "Fabrication of a hybrid PDMS/SU-8/quartz microfluidic chip for enhancing UV absorption whole-channel imaging detection sensitivity and application for isoelectric focusing of proteins," Lab Chip **9**, 1926–1932 (2009).
32. B. Dang, M. S. Bakir, and J. D. Meindl, "Integrated thermal-fluidic I/O interconnects for an on-chip microchannel heat sink," IEEE Electron Device Lett. **27**, 117–119 (2006).
33. B. Dang, M. S. Bakir, D. C. Sekar, C. R. King, Jr., and J. D. Meindl, "Integrated microfluidic cooling and interconnects for 2D and 3D chips," IEEE Trans. Adv. Pack. **33**, 79–87 (2010).
34. P. Bienstman, "Rigorous and efficient modelling of wavelength scale photonic components," Ph.D. dissertation (Ghent University, 2001).